Astronomy & Astrophysics manuscript no. output
November 23, 2020

The GAPS programme at TNG,⋆

XXIX. Atmospheric Rossiter-McLaughlin effect and atmospheric dynamics of KELT-20b

M. Rainer[1], F. Borsa[2], L. Pino[3,1], G. Frustagli[2,4], M. Brogi[5,6,7], K. Biazzo[8], A. Bonomo[6], I. Carleo[9,10], R. Claudi[10], R. Gratton[10], A.F. Lanza[11], A. Maggio[12], J. Maldonado[12], L. Mancini[13,14,6], G. Micela[12], G. Scandariato[11], A. Sozzetti[6], N. Buchschacher[15], R. Cosentino[17], E. Covino[16], A. Ghedina[17], M. Gonzalez[17], G. Leto[11], M. Lodi[17], A.F. Martinez Fiorenzano[17], E. Molinari[18], M. Molinaro[19], D. Nardiello[20,10], E. Oliva[1], I. Pagano[11], M. Pedani[17], G. Piotto[21], and E. Poretti[17]

(Affiliations can be found after the references)

Received <date>; accepted <date>

ABSTRACT

Context. Transiting ultra-hot Jupiters are ideal candidates to study the exoplanet atmospheres and their dynamics, particularly by means of high-resolution, high signal-to-noise ratio spectra. One such object is KELT-20b, orbiting the fast rotating A2-type star KELT-20. Many atomic species have already been found in its atmosphere, with blueshifted signals that hints at the presence of a day-to-night side wind.

Aims. We aimed to observe the atmospheric Rossiter-McLaughlin effect in the ultra-hot Jupiter KELT-20b, and to study any variation of the atmospheric signal during the transit. For this purpose, we analysed five nights of HARPS-N spectra covering five transits of KELT-20b.

Methods. We computed the mean line profiles of the spectra with a least-squares deconvolution using a stellar mask obtained from the Vienna Atomic Line Database ($T_{\rm eff}$=10 000 K, log g=4.3), and then we extracted the stellar radial velocities by fitting them with a rotational broadening profile in order to obtain the radial velocity time-series. We used the mean line profile residuals tomography to analyse the planetary atmospheric signal and its variations. We also used the cross-correlation method to study an already known double-peak feature in the FeI planetary signal.

Results. We observed both the classical and the atmospheric Rossiter-McLaughlin effect in the radial velocity time-series. The latter gave us an estimate of the radius of the planetary atmosphere that correlates with the stellar mask used in our work (R_{p+atmo}/R_p = 1.13 ± 0.02). We isolated the planetary atmospheric trace in the tomography, and we found radial velocity variations of the planetary atmospheric signal during transit with an overall blueshift of ≈ 10 km s^{-1}, along with variations in the signal's depth and full width at half maximum (FWHM). We also find a possible variation in the structure and position of FeI signal in different transits.

Conclusions. We confirm the previously detected blueshift of the atmospheric signal during the transit. The FWHM variations of the atmospheric signal may be caused by more turbulent condition at the beginning of the transit, or by a variable contribution of the elements present in the stellar mask to the overall planetary atmospheric signal, or by iron condensation. **The FeI signal is highly variable from one transit to the other.**

Key words. planetary systems – techniques: spectroscopic – techniques: radial velocities – planets and satellites: atmospheres – stars: individual: KELT-20

1. Introduction

A very interesting category of exoplanets is represented by the transiting ultra-hot Jupiters (UHJs; Bell & Cowan 2018), which are highly irradiated Jupiter-size planets with day-side temperatures higher than 2200 K (Parmentier et al. 2018). Transiting UHJs are ideal laboratories to study planetary atmospheres: their inflated atmospheres and high equilibrium temperatures ($T_{\rm eq}$) result in strong signals and striking peculiar conditions for a planetary body. Their atmospheres are rich in atomic and molecular species: for example, CrII, FeI, FeII, MgII, NaI, ScII, TiII, and YII have been detected in KELT-9b, the hottest UHJ known so far ($T_{\rm eq}$ = 4050 K), with additional evidence of the presence of CaI, CrI, CoI, and SrII (Hoeijmakers et al. 2018, 2019). Because of the presence of neutral and ionized iron in their atmospheres, UHJs can be used to study the atmospheric Rossiter-McLaughlin effect (Borsa et al. 2019): in fact the signal coming from their atmosphere correlates with the stellar mask used to compute the mean line profile of the spectra and recover the star's radial velocity (RV), resulting in an additional absorption in the mean line profile that causes an apparent RV variation similar to the classical Rossiter-McLaughlin effect (RML). In addition to that, UHJs have usually very different atmospheric conditions (*e.g.*, in temperature and chemical composition) between day and night side, that may result in day-to-night side wind (Ehrenreich et al. 2020; Heng & Showman 2015): high resolution spectroscopy may be used to study the RV variations of the atmospheric signal in order to search for the presence of winds or any other kind of atmospheric turbulence.

KELT-20b (Lund et al. 2017), *aka* MASCARA-2b (Talens et al. 2018), is a well known ultra-hot Jupiter orbiting a fast rotating A-type star. With a period of 3.47 days and a semi-major axis of 0.0542 au, KELT-20b is highly irradiated by its host star (A2, $T_{\rm eff}$ = 8980 K, m_V = 7.6) and its atmosphere reaches $T_{\rm eq}$ = 2260 K (see Table 1 for more details on the system).

Many atomic species such as FeI, FeII, CaII, NaI, HI have been detected in its atmosphere through transit spectroscopy,

⋆ Based on observations made with the Italian Telescopio Nazionale Galileo (TNG) operated by the Fundación Galileo Galilei (FGG) of the Istituto Nazionale di Astrofisica (INAF) at the Observatorio del Roque de los Muchachos (La Palma, Canary Islands, Spain).

Table 1. Physical and orbital parameters of the KELT-20 system (*aka* MASCARA-2, *aka* HD185603)

Parameter	Symbol	Value
Stellar Parameters		
Spectral type [1]		A2
V-band magnitude [2]	m_V	7.6
Effective temperature [3]	$T_{\rm eff}$	8980^{+90}_{-130} K
Projected rotation speed [4]	$v \sin i_\star$	116.23 ± 1.25 km s^{-1}
Linear limb darkening [1]	u	$0.532^{+0.011}_{-0.014}$
Surface gravity [3]	$\log g$	4.31 ± 0.02 cgs
Metallicity [3]	[Fe/H]	-0.02 ± 0.07 dex
Stellar mass [3]	$M_\star$	$1.89^{+0.06}_{-0.05}\ M_\odot$
Stellar radius [3]	$R_\star$	$1.60 \pm 0.06\ R_\odot$
Rotation period [4]	$p_\star$	0.695 ± 0.027 days
Planetary parameters		
Planet mass [1]	M_p	$< 3.51\ M_{\rm Jup}$
Planet radius [3]	R_p	$1.83 \pm 0.07\ R_{\rm Jup}$
Planet-to-star ratio [1]	$R_p/R_\star$	$0.11440^{+0.00062}_{-0.00061}$
Planet-to-star ratio [3]	$R_p/R_\star$	0.115 ± 0.002
Equilibrium temperature [3]	$T_{\rm eq}$	2260 ± 50 K
Surface gravity [1]	$\log g_{\rm p}$	< 3.46 cgs
Overall Fe volume mixing ratio (solar value) [5]	$\log {\rm VMR_{Fe}}$	-4.27 cgs
Orbital parameters		
Epoch [3]	T_P	$2\,457\,909.5906^{+0.0003}_{-0.0002}$ BJD
Period [3]	P	$3.474119^{+0.000005}_{-0.000006}$ days
Transit duration [1]	$T_{\rm dur}$	$0.14882^{+0.00092}_{-0.00090}$ days
Semi-major axis [1]	a	$0.0542^{+0.0014}_{-0.0021}$ au
Inclination [1]	i	$86.15^{+0.28}_{-0.27}$ deg
Eccentricity	e	0 (fixed)
Projected obliquity [3]	λ	0.6 ± 4 deg
Stellar RV amplitude [6]	K_s	322.51 m s^{-1}
Systemic velocity [1]	$V_{\rm Sys}$	-23.3 ± 0.3 km s^{-1}
Systemic velocity [3]	$V_{\rm Sys}$	-21.3 ± 0.4 km s^{-1}
Systemic velocity [7]	$V_{\rm Sys}$	-22.06 ± 0.35 km s^{-1}
Systemic velocity [4]	$V_{\rm Sys}$	-24.48 ± 0.04 km s^{-1}

References. [1] Lund et al. (2017); [2] Høg et al. (2000); [3] Talens et al. (2018); [4] this work; [5] Asplund et al. (2009); [6] Casasayas-Barris et al. (2019); [7] Nugroho et al. (2020)

while there are only tentative detections of MgI and CrII (Casasayas-Barris et al. 2018, 2019; Hoeijmakers et al. 2020; Nugroho et al. 2020; Stangret et al. 2020). There are also hints of the presence of a day-to-night side wind due to the presence of a blueshift of -6.3 ± 0.8 km s^{-1} in the FeI signal, and -2.8 ± 0.8 km s^{-1} in that due to FeII (Stangret et al. 2020; Hoeijmakers et al. 2020; Nugroho et al. 2020).

We observed KELT-20 in the framework of the Global Architecture of Planetary Systems (GAPS) project, which is an Italian project dedicated to the search and characterization of exoplanets (PI G. Micela; Covino et al. 2013). Particularly, one of GAPS' main lines of research focuses on the study of exoplanets' atmospheres using both transmission and emission spectroscopy (Borsa et al. 2019; Pino et al. 2020; Guilluy et al. 2020). Using both our data and public data of KELT-20 taken with the same instrument (HARPS-N), we studied both the classical (Rossiter 1924; McLaughlin 1924) and atmospheric RML effects of KELT-20b from the RV time-series, along with the variations of the atmospheric trace during the planetary transits from the mean line profile tomography.

The dataset used in this work is described in Sec. 2, while the method used to obtain the mean line profiles and the RV time-series is detailed in Sec. 3. Both the classical and atmospheric RML effects are shown in Sec. 4. The variations of the atmospheric trace during the transit and the methods used to detect them from the mean line profile tomography are described in Sec. 5. In Sec. 6 we describe the cross-correlation with a FeI model performed in order to compare our results with those found in the literature. Finally, our conclusions are in Sec. 7.

2. Data sample

We analysed five transits of KELT-20b observed with the high-resolution echelle spectrograph HARPS-N (Cosentino et al. 2012) installed at the Telescopio Nazionale Galileo (TNG) at the Roque de los Muchachos Observatory (La Palma, Spain). HARPS-N is an optical spectrograph with resolving power R = 115 000 and wavelength coverage 383-693 nm. It is a twin of the HARPS spectrograph installed at the 3.6m telescope of the ESO-LaSilla Observatory, down to the Data Reduction Software (DRS) optimized for exoplanet search.

We observed two transits (2019-08-26 and 2019-09-02) in the framework of the GAPS programme, while the other three transits are public data retrieved from the HARPS-N archive

Table 2. Data

Night	# of spectra	T_{exp}	Mean S/N
2017-08-16	90	200s	61
2018-07-12	116	200s	93
2018-07-19	78	300s	105
2019-08-26	30	600s	164
2019-09-02	29	600s	176

(2017-08-16: PID CAT17A_38 PI Rebolo; 2018-07-12, and 2018-07-19: PID CAT18A_34, PI Casasayas-Barris). The GAPS observations were taken in the GIARPS mode (Claudi et al. 2016), that allows the simultaneous use of both HARPS-N and GIANO-B (Oliva et al. 2012; Origlia et al. 2014) spectrographs. GIANO-B is an high-resolution (R = 50 000) near-infrared echelle spectrograph covering the wavelength range from 950 to 2450 nm. For this work, we used only the HARPS-N data

A summary of the acquired HARPS-N spectra in the five transit nights is shown in Table 2. We rejected 14 spectra taken during the night 2018-07-12 because of their low S/N. All five transits are complete, and out-of-transit spectra were taken both before and after the transit in each night. We worked on spectra reduced by the HARPS-N DRS (Cosentino et al. 2014), as such the barycentric correction was already applied.

3. Mean line profiles

While the HARPS-N DRS is a very powerful tool, it is not optimized for hot stars such as KELT-20: the resulting cross-correlation functions (CCFs) are obtained by using a stellar mask designed to work with a G2-type star, *i.e.* the hottest stellar mask available in the DRS mask library.

We decided then to compute the mean line profile using the Least-Squares Deconvolution software (LSD, Donati et al. (1997)) with a stellar mask obtained from the VALD3 database[1] (Piskunov et al. 1995; Ryabchikova et al. 2015). We downloaded stellar masks for $T_{\rm eff}$=9000 K and $T_{\rm eff}$=10 000 K, both with $\log g$=4.31, solar metallicity, and micro-turbulence v=2 km s^{-1} and wavelength range 3900-7000 Å. While our results are in good agreement using both masks, we show here only those obtained with $T_{\rm eff}$=10 000 K, where both the stellar and the planetary signals are stronger (see Fig. 1, where the $T_{\rm eff}$=10 000 K profile is almost twice as deep as the $T_{\rm eff}$=9000 K one). This may hint at an higher $T_{\rm eff}$ for **KELT-20** then previously found.

To apply the LSD, we first normalized all our spectra using a self-developed automated procedure (Rainer et al. 2016). Then, in order to avoid most of the telluric lines contamination and the heavy contribution of the stellar Balmer lines (extremely strong as expected from KELT-20 spectral type, and with a different shape), we cut them, and we kept only the wavelength ranges 4415-4805, **4915-5870**, 6050-6265, and 6335-6450 Å. We run the LSD software on each individual spectrum to obtain the mean line profiles.

We fitted all the mean line profiles with a rotational broadening function (see Fig. 1), using the formula in Eq. 1 (Gray 2008):

$$f(x) = 1 - 2a(1-u)\sqrt{1-\left(\frac{x-x_0}{x_l}\right)^2} + \frac{0.5\pi u\left[1-\left(\frac{x-x_0}{x_l}\right)^2\right]}{\pi x_l\left(1-\frac{u}{3}\right)}, \quad (1)$$

[1] http://vald.astro.uu.se

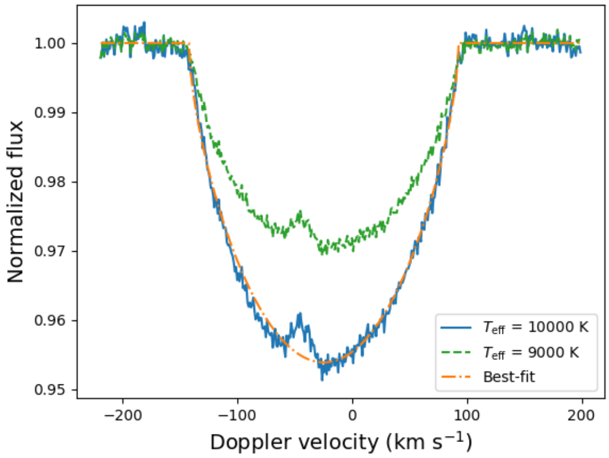

Fig. 1. Mean line profile of a single KELT-20 spectrum obtained with the LSD software and $T_{\rm eff}$=10 000 K (solid blue line) along with the rotational broadening fit (dashed-dotted orange line). For comparison, the mean line profile of the same spectrum with the $T_{\rm eff}$=9000 K is shown (dashed green line). The planet's Doppler shadow is clearly visible as a bump in both lines.

where a is the depth of the profile, x_0 the center (*i.e.*, the RV value), x_l the $v \sin i_\star$ of the star, u the linear limb darkening (LD) coefficient (listed in Table 1). We thus recovered both the RVs and the projected rotational velocities ($v \sin i_\star$) for all observed spectra. We found $v \sin i_\star = 116.7 \pm 0.7$ km s^{-1} by averaging the $v \sin i_\star$ of all the out-of-transit spectra. We did not use here the in-transit ones in order to avoid the Doppler shadow affecting our result.

We also computed the $v \sin i_\star$ using the Fourier transform method (Smith & Gray 1976; Dravins et al. 1990): because of the fast rotation of KELT-20 we could use the first three zero positions of the Fourier transform of all our mean line profiles to derive the projected rotational velocity. Using only the out-of-transit spectra, we found an average value of $v \sin i_\star$ = 116.23 ± 1.25 km s^{-1}, which aligns well with that obtained by the profile fitting. We note here that, in case of such a fast rotating star, this method is independent from other broadening effects as for example macro-turbulence, and it only depends on the LD coefficient: for this reason, we report this value in Table 1, even if the error is larger than that obtained with the profile fitting. The average value of the ratio of the first two zero positions results in $q_2/q_1 = 1.805 \pm 0.036$, which is compatible with a rigid rotation ($1.72 < q_2/q_1 < 1.83$, Reiners & Schmitt (2002)).

We computed the stellar rotational period as $p_\star = 2\pi R_\star / v_{\rm eq}$, using $R_\star$, $v \sin i_\star$, and inclination i from Table 1. We considered the orbit inclination i equal to the stellar inclination $i_\star$, seeing as the projected obliquity λ is compatible with a zero value. We found a stellar rotational period of 0.695 ± 0.027 days, which is almost exactly one fifth of the planetary period: this may suggests a resonance between the stellar and planetary rotation.

We performed a linear fit on all the out-of-transit RVs to recover the systemic velocity, and we found $V_{\rm Sys} = -24.48 \pm 0.04$ km s^{-1}. This value is slightly lower than those found in the literature (see Table 1), but the determination of the systemic velocity may vary depending on the instrument and method used to estimate it. We also computed $V_{\rm Sys}$ independently on the five nights, and we noted a small, but significant downwards trend that may be worth keeping in mind in further studies (see Fig. 2).

In Fig. 3 we show the RVs corrected for the different $V_{\rm Sys}$ (so that five nights aligns on the average $V_{\rm Sys}$ value),

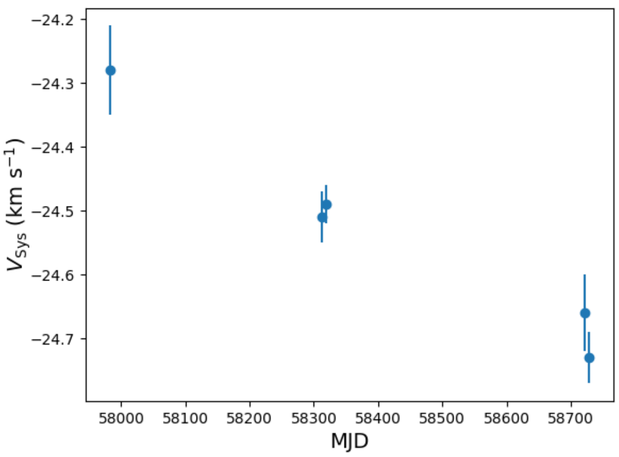

Fig. 2. Systemic velocity of the five nights: a small downwards trend is clearly visible.

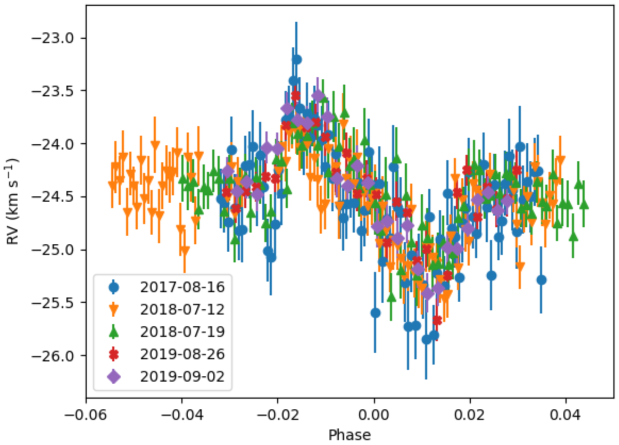

Fig. 3. RVs data phase-folded using the KELT-20b known orbital period (P = 3.474119 days). **The RV values were shifted by the difference between the individual V_{Sys} of each night and the average V_{Sys} value to account for the trend found in our data.**

and phase-folded using the known orbital value of KELT-20b (P = 3.474119 days, see Table 1). The RML effect is clearly visible.

4. Classical and atmospheric RML effects

The RML effect is visible in all nights of observations (see Fig. 3). We averaged the phase-folded RVs data of all transits using a 0.002 phase bin and we compared them with a theoretical model obtained using the already known system parameters of Table 1, using our value for the systemic velocity. The RML model was computed with the `Rmcl` model class of the PyAstronomy[2] package (Czesla et al. 2019) of Python[3] (Van Rossum & Drake Jr 1995), which implements the analytical model RV curves for the RML effect given by Ohta et al. (2005).

The comparison between the data and the theoretical model is shown in Fig. 4: the model seems to overestimate the amplitude of the RML effect, but we know from a previous study on KELT-9b (Borsa et al. 2019) that the atmospheric RML effect may combine with the classical RML effect and the resulting RVs carry both signals.

[2] https://github.com/sczesla/PyAstronomy
[3] http://www.python.org

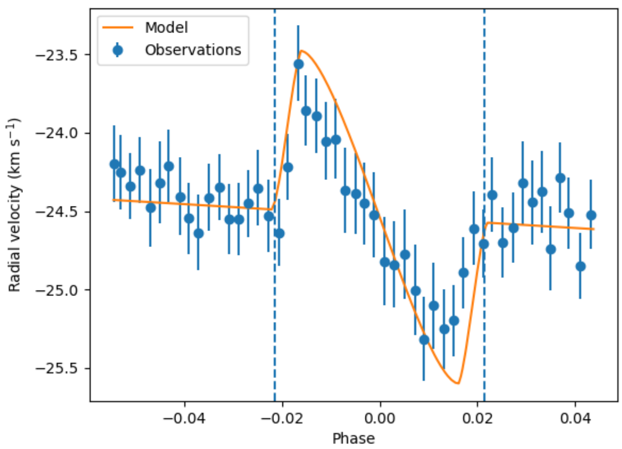

Fig. 4. Comparison between the observed RVs averaged with 0.002 phase bin (blue points) and the RML RV model (orange line). The model seems to overestimate the amplitude of the RML effect, while actually the atmospheric RML effect is lowering the amplitude of the signal. The vertical dashed lines show the transit's ingress and egress.

The atmospheric RML effect is akin to the classical one, *i.e.* an apparent stellar RV variation due to the deformation of the stellar lines. While in the classical RML effect the deformation is caused by the occultation of part of the stellar disk by the transiting planet, in the atmospheric RML effect we have an additional absorption signal due to the planetary atmospheric spectrum correlating with the mask used to compute the CCF or the LSD mean line profile. This happens only in the case of extremely hot planetary atmospheres, that show a chemical composition similar to that of late-type stars (in particular due to the presence of neutral or ionized iron), and as such their atmospheric spectrum correlates with the same mask used for the host stars (*e.g.*, in this case the stellar mask contains most of the elements found in the atmosphere of KELT-20b, with more than half of the lines being either `FeI` or `FeII`).

Looking at the line profile residuals tomography (Fig. 5, see Section 5 for details), not only the Doppler shadow is visible (red hues), but also the planetary atmospheric trace (blue hues). The latter shifts by the change in planet's orbital RV during transit, confirming that the planet's atmospheric spectrum is correlating with the stellar mask, and thus it shows up in the line residuals as an additional absorption line situated at the planet RV. The Doppler shadow and the atmospheric trace are aligned in such a way that the atmospheric trace is expected to affect the RVs derived from the mean line profiles in the opposite way than the Doppler shadow, so that the net result would be a smaller amplitude of the RML effect, as it is actually seen in Fig. 4.

We then subtracted the RML theoretical model from our data: the resulting RV residuals show the atmospheric RML effect. It goes in the opposite direction from the classical RML effect because it modifies the line profile as an additional absorption instead of a bump. We fit the RV residuals (see Fig. 6) using the `Rmcl` fit class of the same PyAstronomy package used before. We interpret the resulting value $R_p/R_\star = 0.060 \pm 0.002$ given by the fit as $R_{atmo}/R_\star$, where R_{atmo} represents the extension of the atmosphere that correlates with the stellar mask that we used, if the atmosphere were shaped as a disk. The error on this value was estimated using the `pymc`[4] package of Python. Comparing this result with the planet's radius $R_p/R_\star = 0.115 \pm 0.002$, the atmospheric area is $\sim$ 27% of the whole planetary photometric area.

[4] https://github.com/pymc-devs/pymc

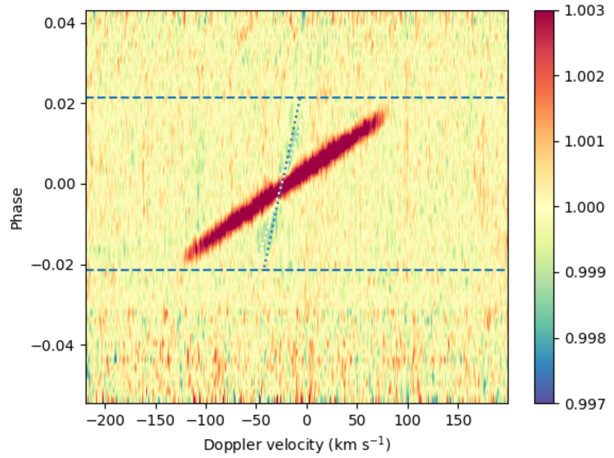

Fig. 5. Mean line profile tomography: the average stellar line has been removed, but not the systemic velocity. In the residuals both the Doppler shadow (red excess) and the atmospheric trace (blue absorption, evidenced by the blue dotted line) are visible.

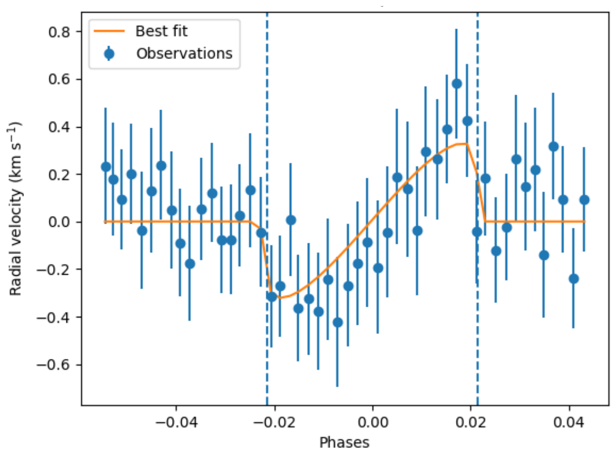

Fig. 6. RVs residuals show the atmospheric RML effect. The overplotted orange line shows the RML model best fit.

If we hypothesize the most simple scenario of a spherical atmosphere, we can then derive $R_{p+atmo} = 1.13 \pm 0.02\, R_p$, only for the portion of the planetary atmosphere whose spectrum correlates with the stellar mask. **This value is in good agreement with the results from Casasayas-Barris et al. (2019), who found $R_{p+atmo} = 1.11 \pm 0.03\, R_p$ for FeII. The slightly larger value found here may be due to the presence of few lines of other elements, *e.g.* CaII, for which Casasayas-Barris et al. (2019) found $R_{p+atmo} = 1.19 \pm 0.03\, R_p$.**

We note here that adjusting the classical RML theoretical model by varying the system parameters values inside their error ranges alters only slightly our atmospheric RML result, which remains in agreement with the $R_{atmo}/R_\star = 0.060 \pm 0.002$ value within the 1σ uncertainty.

5. Atmospheric trace

We studied the planetary atmospheric trace **following the same strategy used with the RVs in Sec. 4, and applying it to the mean line profiles: we combined** all five transits, in order to increase the strength of the atmospheric signal and to average out spurious variations due to instrumental or telluric effects.

We averaged all our out-of-transit mean line profiles to obtain a purely stellar mean line profile. Because KELT-20 does not show any significant stellar variations, either due to activity or pulsations, we could then remove the stellar component from our data simply by dividing each mean line profile (both in and out of transit) by the average out-of-transit stellar mean line profile. **We then normalized the residuals by dividing them using two different linear fits, one for the points outside the stellar line limits, the other for the points inside the stellar line limits. The latter fit was done avoiding the regions where the Doppler shadow or the atmospheric trace are present.** The resulting residuals are shown in Fig. 5; to enhance the signal's visibility they are binned with a 0.002 phase bin and a **1 km s^{-1} RV bin**.

To isolate and investigate possible variations of the atmospheric trace during transit, we had to remove the Doppler shadow. To be sure that the removal process did not influence our analysis, we proceeded in two different ways:

a) by **following the method of Hoeijmakers et al. (2019): we selected the residuals where the Doppler shadow signal is far from the atmospheric trace and we fitted it with a Gaussian. Then we fitted the Gaussian parameters with a 2nd order polynomial, so that the fit parameters of the Doppler shadow vary smoothly during the transit. We then removed the Doppler shadow Gaussian model from all the residuals.**
We note here that we obtained a better removals by first shifting all our data in the reference frame of the Doppler shadow, probably because of the geometry of the KELT-20 system. We did this using the estimated Doppler shadow RV obtained from Eq. 2 (Cegla et al. 2016):

$$rv = v \sin i_\star \left(x_p \cos\lambda - y_p \sin\lambda \right), \quad (2)$$

where:

$$x_p = a_{R_\star} \sin 2\pi\phi,$$

$$y_p = -a_{R_\star} \cos 2\pi\phi \cos i,$$

with λ the projected obliquity in radians, $a_{R_\star}$ the semi-major axis in units of stellar radius, ϕ the orbital phase and i the orbital inclination in radians. After this, our Doppler shadow signal was vertically aligned, and we proceeded with the removal as described above;

b) by adopting and adjusting the method from Cabot et al. (2020). The original method was applied to the UHJ WASP-121b, which orbits in a near-polar orbit around its host star ($\lambda = 257.8^{+5.3}_{-5.5}$ deg; Delrez et al. 2016). Because of this, its Doppler shadow in the stellar reference frame is almost completely vertically aligned at the center of the stellar line profile. Cabot et al. (2020) removed it by fitting a 3rd degree polynomial on each column of the tomography where the Doppler shadow fell.
Because of the different geometry of the KELT-20 system, we had to modify this approach to suit our data. First of all, we shifted the data in the reference frame of the Doppler shadow as in the original work of Cabot et al. (2020). We could then fit the columns where the Doppler shadow signal fell, and finally we divided each column by its fit. We used a 5th degree polynomial, instead of the original 3rd degree one, because it performed a better removal of the Doppler shadow.

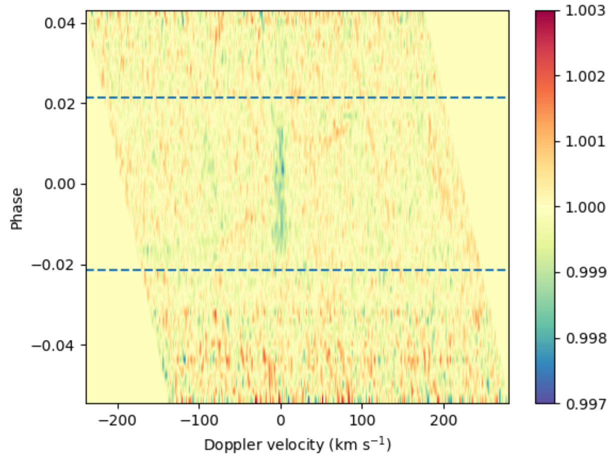

Fig. 7. Line profile residuals after the Doppler shadow removals, and after being shifted in the planet reference frame. The atmospheric trace is clearly visible and centered around 0 km s^{-1}.

We obtained thus two datasets: dataset A, where the Doppler shadow was removed by Gaussian fitting, and dataset B, where the Doppler shadow was removed adapting the Cabot et al. (2020) method. **Because the results we obtained with the two datasets are in good agreement, we show here only the work done on dataset A, while the results from dataset B are presented in appendix A.**

Once removed the Doppler shadow signal, we shifted the dataset in the planet reference frame, *i.e.* we shifted each spectrum by the combination of V_{Sys} and the planet theoretical orbital RV (the barycentric correction was already applied by the HARPS-N DRS), in order to align the atmospheric signal in a vertical position around 0 km s^{-1} and to better study its variations (see Fig. 7).

We then considered each mean line profile to map the velocity variations during transit. Because the atmospheric signal is not very strong, we applied a Savitzky-Golay filter (Savitzky & Golay 1964) to each profile in order to smooth out the noise and **increase the signal's visibility**. The Savitzky-Golay filter works by computing a least-squares low-degree polynomial fit (3^{rd} degree in our case) in a moving window on the data to estimate the value of the central point of each window, and it is able to smooth the data without greatly distorting the signal. **While it was originally created for spectroscopic chemistry, the Savitzky-Golay filter has been successfully applied to several kind of spectroscopic astronomical data (*e.g.*, Deetjen 2000; Dimitriadis et al. 2019; Fleig et al. 2008).** We applied the Savitzky-Golay filter by using the `savgol_filter` function of SciPy[5] **with an optimal window width of 15 pixel. We obtained the window value by applying the method proposed by Sadeghi & Behnia (2018) to our data**.

After applying the Savitzky-Golay filter, **we fitted the atmospheric signal with a Markov-Chain MonteCarlo (MCMC) sampling and a correlated noise model using Gaussian processes. In order to do this, we used the Python packages `emcee`[6] (Foreman-Mackey et al. 2013) and `george`[7] for the noise model. In Fig. 8 we show 24 random posteriors for each of the 20 mean line profile residuals that we have during the transit.**

The fit results are shown in Fig. 9. There is a RV change during transit with roughly a 10 km s^{-1} span: the signal remain stable for most of the transit, and then it blueshifts during egress. Aside from one outlier, the FWHM is more stable, even if it seems to increase just after ingress. Additionally, there is more scatter in the FWHM values in the first half of the transit than in the second half. The depth of the signal increases from the beginning to the center of the transit, and then it decreases in a roughly symmetric way.

Averaging the residuals in the first and the second half of the transit (phases [-0.02:0.0] and [0.0:0.02], see Fig. 10) **shows a larger FWHM value in the first half of the transit, but the results are compatible within 1σ.** The depth variation is cancelled out within 1σ, and also the RV variation in the averaged signals disappears within 1σ. The latter is due to the fact that the major RV variation is caused only by the last three points, where the atmospheric signal is smaller (see last panels of Fig. 8) and as such their contribution to the average is lower.

We tried to study the atmospheric trace behaviour in each transit, but the S/N was too low to allow us to follow the finer variations shown in Fig. 9. However, we were able to determine the overall variations between the first and second half of the transits, and we found **interesting results (see Fig. 11). The FWHM increases during the transit on 2017-08-16, then it decreases but within or just above 1σ on 2018-07-12 and 2018-07-19, while it significantly decreases on 2019-08-26 and 2019-09-02. The signal's depth is more stable, aside from 2019-08-26 where it visibly decreases from the first to the second half of the transit. The RVs is stable during two nights (2017-08-16, and 2018-07-19), it blueshifts on 2018-07-12, and it redshifts on 2019-08-26, and 2019-09-02. We found different behaviour of the atmospheric trace during different transits. Overall, the FWHM decreases during the transit, as it has been observed in four nights out of five.**

It is interesting to note that a significant variation of FWHM has been found between the elements detected in the atmosphere of KELT-20b by Hoeijmakers et al. (2020), varying from 5.31±0.99 km s^{-1} for `CrII` to 33.45±3.30 km s^{-1} for `MgI`. Because our planetary atmospheric trace is obtained through the use of a stellar mask (where several different elements are combined), one possible interpretation for our FWHM variations could arise from a variable contribution of the chemical elements during the transit, due for example to temperature variations that may cause some of them to condense. Still, because `FeI` and `FeII` constitute more than half of the mask's lines, **another possible** cause may be the condensation of iron, similarly to what happens in the UHJ WASP-76b (Ehrenreich et al. 2020). Another interpretation could be the presence of more turbulent atmospheric conditions in the first part of the transit, due for example to a day-to-night side wind, as has been found also in both WASP-76b (Ehrenreich et al. 2020) and WASP-121b (Bourrier et al. 2020).

We stress here that the atmospheric RV variations of KELT-20b are not visible when studying only the first and second half of the transit, even when combining all five transits data (see Fig. 10 and Fig. 11), but they are quite clearly visible when tracing the finer atmospheric variations (see Fig. 8 and Fig. 9). Due to the faintness of the signal, this study is possible only in the combined data.

6. Cross-correlation with FeI models

Nugroho et al. (2020) detected several elements in the atmosphere of KELT-20b through the CCF method, and they found a peculiar double-peak shape in the $K_p - \Delta V$ maps of `FeI`. The

[5] https://www.scipy.org
[6] https://emcee.readthedocs.io/en/stable/
[7] https://george.readthedocs.io/en/latest/

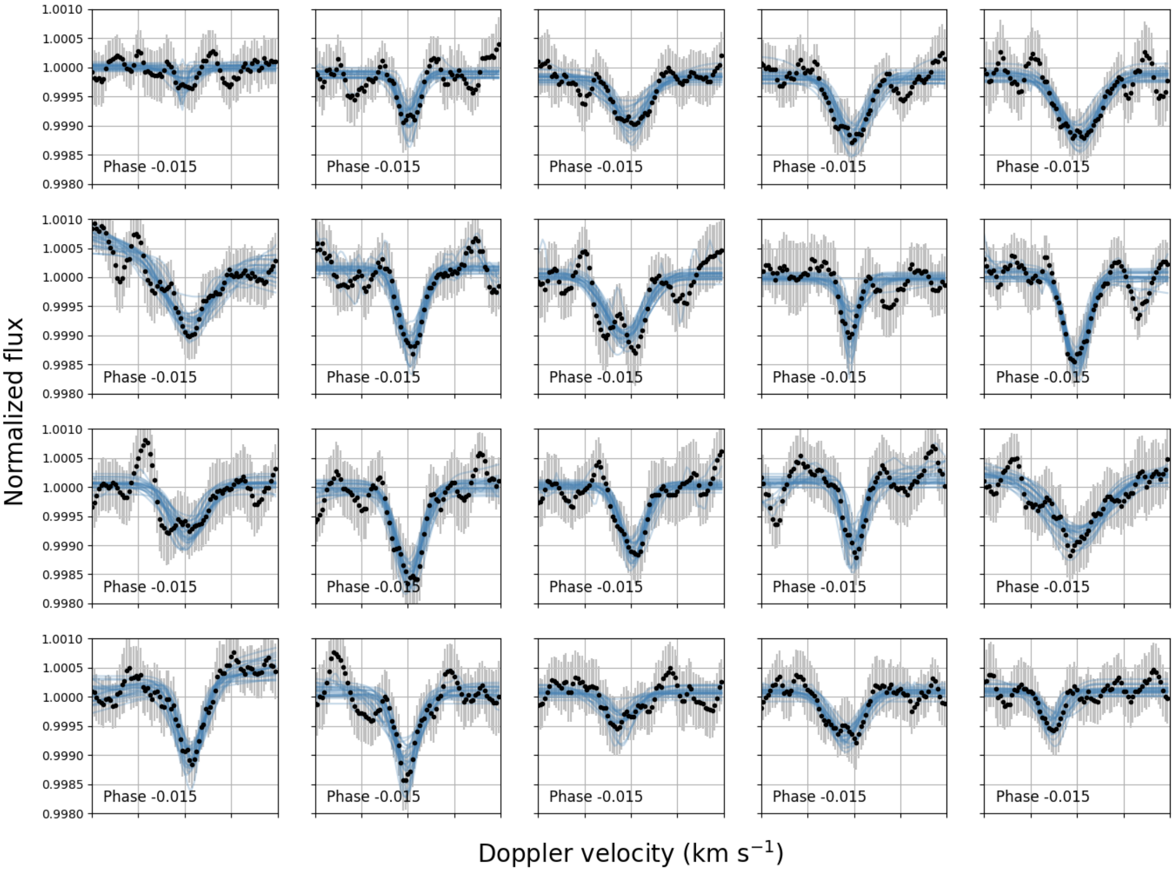

Fig. 8. Atmospheric signal and relative MCMC posteriors. All the graphics have the same abscissa (RVs from -40 to 40 km s^{-1}) and ordinate (normalized flux from 0.998 to 1.001) to better follow the evolution of the signal. The graphics go from phase -0.019 (upper left panel) to phase 0.019 (lower right panel) with a 0.002 phase step.

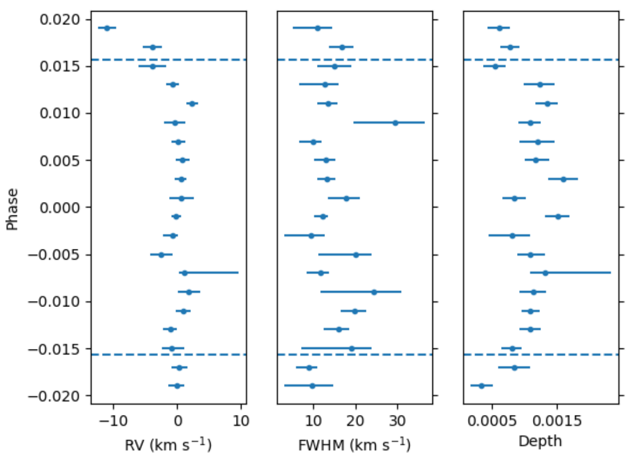

Fig. 9. RVs, FWHM and depth of the atmospheric signal during transit. Description and tentative interpretation of the variations in the text. All the data are comprised between t_0 (start of ingress) and t_2 (end of egress), while the dashed lines indicate t_2 (end of ingress) and t_3 (start of egress)

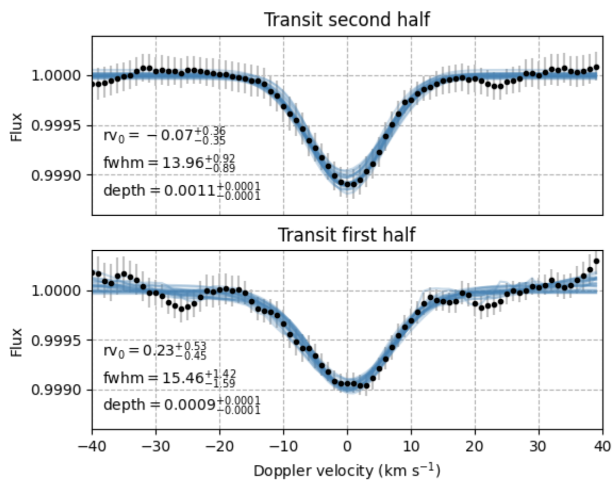

Fig. 10. Averaged atmospheric signal in the first (phase [-0.02:0.0]) and second part (phase [0.0:0.02]) of the transit **with relative fit.**

peaks have similar K_p, and they are roughly ≈ 10 km s^{-1} apart, with the secondary blueshifted peak weaker than the primary one. They reconstructed the observed structure by simulating two `FeI` signals with different amplitudes and ΔV, and found the best match when masking the weaker signal (at ΔV = -10

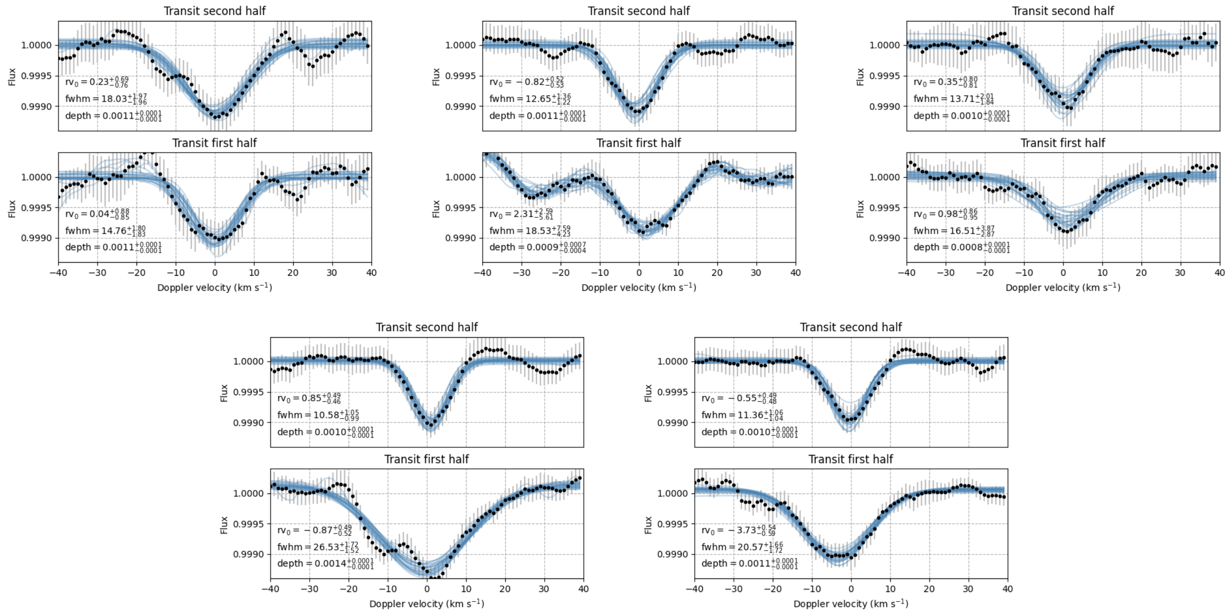

Fig. 11. Averaged atmospheric signal in the first (phase [-0.02:0.0]) and second part (phase [0.0:0.02]) of each transit. From top left to bottom right, the graphics show the results for the nights 2017-08-16, 2018-07-12, 2018-07-19, 2019-08-26, and 2019-09-02.

km s^{-1}) from phase -0.01 and -0.016, simulating a delay in its appearance. This behaviour closely resembled what we observed in the planetary atmospheric RV variations, with a blueshifted signal in the final part of the transit (see Fig. 9).

Since they used the same HARPS-N observations for the 2017-08-16, 2018-07-12, and 2018-07-19 transits, and we have two additional HARPS-N nights (2019-08-26 and 2019-09-02) that were not used in their work, we decided to look for the same double-peak signature in our data. We could not use directly our LSD results, because the stellar mask contains several different elements aside from `FeI`, so we decided to apply the CCF method to obtain our own $K_p - \Delta V$ maps.

To create our model, we employed the $^{\pi}\eta$ line-by-line radiative transfer code (Ehrenreich et al. 2006, 2012; Pino et al. 2018). This code was already used for the simultaneous interpretation of HARPS high-resolution spectroscopic observations and HST WFC3 observations (Pino et al. 2018). For this paper, we updated the code to include:

1) line opacities from `FeI` and a continuum by H^- following Pino et al. (2020). The `FeI` lines were taken from the VALD3 database[8], and modelled as Voigt profiles, accounting for thermal and natural broadening.

2) equilibrium chemistry calculations for `FeI` and H^-, to calculate their volume mixing ratios throughout the atmosphere. We employed the publicly available `FastChem` code version 2 (Stock et al. 2018).

We employed a fixed temperature profile from Lothringer & Barman (2019), representative for a $T_{\rm eq}$ = 2250 K planet orbiting around an F0-type star ($T_\star$ = 7200 K). The other parameters employed in our model are $R_\star$, M_p, $\log {\rm VMR_{Fe}}$, and R_p at a reference pressure level of 10 bar (see Table 1). Nugroho et al. (2020) demonstrated that the neutral iron lines in KELT-20b can be well represented with a hydrostatic equilibrium model, provided that the model accounts for a scale factor (α in their notation). Our cross-correlation scheme is not sensitive to such a scale factor, which is thus fixed to 1.

We performed a cross-correlation in the stellar restframe between the data and our model on each residual spectrum, after the removal of an out-of-transit stellar master, and telluric contamination (as in Borsa et al. 2020). Our CCFs are defined as in Eq. 3:

$$CCF(v,t) = \sum_{i=1}^{N} x_i(t,v) M_i \tag{3}$$

where x are the N wavelengths of the spectra taken at the time t and shifted at the velocity v, and M is the model normalized to unity. **We impose all the model values smaller than 5% of the maximum absorption line in the considered wavelength range to be at zero (*e.g.*, Hoeijmakers et al. 2019).**

We selected a step of 1 km s^{-1} and a velocity range [-200,200] km s^{-1}. The spectra are divided in segments of 200 Å (*e.g.*, Hoeijmakers et al. 2019), then the cross-correlation is performed for each segment. We masked the wavelength range 5240-5280 Å, which is heavily affected by telluric contamination. Then for each exposure we applied a weighted average between the CCFs of the single segments, where the weights applied to each segment are the sum of the depths of the lines in the model and the inverse of the standard deviation of the segment (*i.e.*, the higher the S/N, the larger the weight). We then averaged all the in-transit CCFs after shifting them in the planetary restframe, for a range of K_p values from 0 to 300 km s^{-1}, in steps of 1 km s^{-1}. The shift is performed by subtracting the planetary RV calculated for each spectrum as $v_p = K_p \times \sin 2\pi\phi$, where ϕ is the orbital phase. As a last step, we subtracted the $V_{\rm Sys}$ from all the averaged CCFs to obtain the $K_p - \Delta V$ maps. We then created S/N maps by computing the standard deviation of each $K_p - \Delta V$ map far from the planetary signal (*i.e.* excluding the region from $V_{\rm Sys}$ = -40 km s^{-1} to $V_{\rm Sys}$ = 40 km s^{-1}), and then dividing the $K_p - \Delta V$ maps by these values.

Our results are shown in Fig. 12: we identified the strongest peak or peaks in each map with a local maxima algorithm.

[8] See Pino et al. (2020)) for a full list of references for the case of `FeI`.

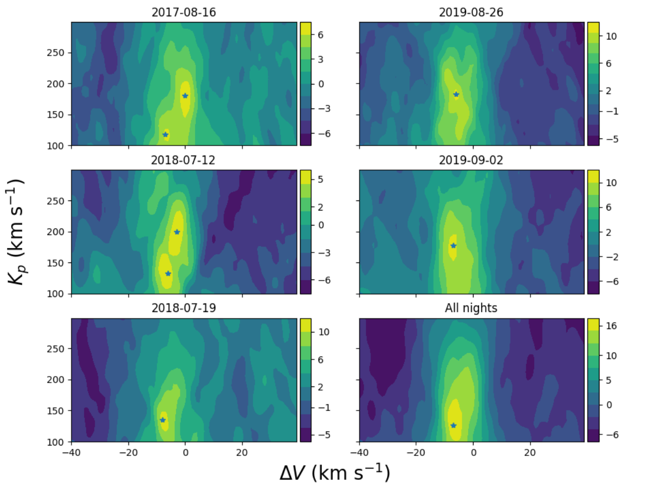

Fig. 12. Contour plots of the $K_p - \Delta V$ maps for the five transit nights and the combined data (bottom right panel). The prominent peaks are indicated with star symbols.

We found the double-peak feature quite clearly in the first two transits (2017-08-16, and 2018-07-12), while only the weaker blueshifted signal is present in the third transit (2018-07-19). We remind that those are the same data analyzed by Nugroho et al. (2020). In the fourth and fifth transits (2019-08-26, and 2019-09-02) only the stronger signal is visible.

To further investigate the variability of the `FeI` signal as a function of transit, we ran MCMC simulations via the Python `emcee` package and drove their evolution via the likelihood scheme of Brogi & Line (2019). Not only does this scheme allow us to account for the level of correlation between model and data (through a cross-covariance term), but also for the overall line amplitude and shape (through the variances of model and data). In these simulations, the likelihood was maximised as a function of four parameters: the two velocities (orbital and systemic), the FWHM of the line profile, and the logarithm of a scaling factor, $\log S$. While the measured systemic velocity is consistent within 1 sigma between the nights (aside from the first night), the other three parameters show a clear variability, as reported in Table 3. Here we redefine K_p as $K_{\rm p+atmo}$, because it combines both the projected orbital velocity of the planet and a contribution from the atmosphere's physics and dynamics.

The results show with a high significance that the values of $K_{\rm p+atmo}$ and $\log S$ are highly variable over the five transits. This means that the dynamics probed by the `FeI` signal, as well as the overall strength of the iron lines, both change from night to night. Furthermore, there is strong evidence that the broadening of the line profile also varies, as shown by the retrieved values of FWHM. We note here that the nights with larger $K_{\rm p+atmo}$ (2019-08-26 and 2019-09-02) are those with the larger FWHM variations of the atmospheric trace between the two half of the transit, while the night 2017-08-16 is the one with the more deviant values, and also the only one where the atmospheric trace shows an increase of the FWHM from the first to the second half of the transit (see Fig. 11). The difference between the values of FWHM found here and those of the atmospheric trace may arise from the fact that the atmospheric trace described in Sec. 5 is caused by a combination of the different elements found in the stellar mask. Additionally, we confirm the blueshift of the `FeI` signal found also in literature (Stangret et al. 2020; Hoeijmakers et al. 2020; Nugroho et al. 2020),

Lastly, we fixed the FWHM and $\log S$ to their best-fitting values for each night, and ran an additional MCMC with the five nights combined. Also this further test did not confirm a possible double solution. The posterior in $K_{\rm p+atmo}$ appears instead single-peaked, and centered at an intermediate value of 142 km s^{-1}.

Table 3. Signal position, and width and model's scale factor in the `FeI` $K_p - \Delta V$ maps

Night	K_p ($K_{\rm p+atmo}$) (km s^{-1})	ΔV (km s^{-1})	FWHM (km s^{-1})	$\log S$
2017-08-16	$99.5^{+13.6}_{-20.2}$	$-1.0^{+1.7}_{-1.4}$	$16.7^{+4.2}_{-2.8}$	$-0.20^{+0.05}_{-0.05}$
2018-07-12	$150^{+13.0}_{-9.1}$	$-3.7^{+1.4}_{-1.3}$	$-9.7^{+2.5}_{-2.6}$	$-0.73^{+0.08}_{-0.09}$
2018-07-19	$129.7^{+4.4}_{-7.2}$	$-6.0^{+0.7}_{-0.6}$	$-6.4^{+3.8}_{-1.9}$	$-0.55^{+0.07}_{-0.06}$
2019-08-26	$163.1^{+21.3}_{-15.2}$	$-3.3^{+0.8}_{-0.9}$	$-12.7^{+1.8}_{-1.8}$	$-0.40^{+0.04}_{-0.05}$
2019-09-02	$161.1^{+4.9}_{-4.9}$	$-4.9^{+0.5}_{-0.5}$	$-9.7^{+1.2}_{-1.2}$	$-0.33^{+0.03}_{-0.03}$
All data	142^{+7}_{-6}	$-4.7^{+0.3}_{-0.3}$		

7. Conclusions

Because of its high $T_{\rm eq}$ (2260 ± 50 K), the atmospheric spectrum of the ultra-hot Jupiter KELT-20b correlates with the stellar mask used to compute the host star mean line profiles. We were thus able to detect and characterize the atmospheric RML effect present in the stellar RV time-series, which resulted in an estimation of the size of the planetary atmosphere that correlates with the mask ($R_{p+atmo}/R_p = 1.13 \pm 0.02$). **This is in agreement with literature values from metal line-depths, confirming the reliability of the atmospheric RML method.** In addition to that, we could isolate the atmospheric trace in the mean line profile tomography: the high-resolution, high S/N of our data allowed us to fit the atmospheric signal and follow its variations during the transit.

We found variations of RV, FWHM and depth of the atmospheric signal during the combined transit data. The greater FWHM spread during the first part of the transit may hint at turbulent conditions, that become more stable in the second part of the transit. This behaviour resembles that found by Ehrenreich et al. (2020) in WASP-76b, and Bourrier et al. (2020) in WASP-121b, and confirms the existence of different structures between morning and evening terminators, as suggested by Hoeijmakers et al. (2020): in their work, they analyzed only one transit and so they could not exclude a spurious nature for the RV variability. With 5 transits showing the same overall pattern (see Fig. 11), plus a detailed study of the combined signal, we confirm the presence of atmospheric dynamics with a progressive blueshift of the signal. Another possible interpretation for the FWHM variations may be the variable contribution of elements to the overall atmospheric signal during the transit: because the stellar mask contains different elements, all of them contribute to the resulting atmospheric trace, but their relative abundances may change during the transit due to, for example, temperature variations that may cause some of them to condense. This may result in a FWHM variation due to the significant FWHM differences between the elements detected in KELT-20b atmosphere (Hoeijmakers et al. 2020). **Seeing as more than half of the stellar mask lines are `FeI` and `FeII` line, the condensation of iron (Ehrenreich et al. 2020) may play a role in this situation.**

The RV variations of the atmospheric trace **led us to explore the results from Nugroho et al. (2020), who found a double-peak feature in their `FeI` K_p–ΔV maps. This feature** consisted of a primary peak at $\Delta V = 0$ km s^{-1} and a weaker secondary peak at ΔV = -10 km s^{-1}. Their best match with simulated signals indicated a delayed appearance of the weaker blueshifted signal, which agrees well with the blueshift we found in the second part of the transit. From our own $K_p - \Delta V$ maps, we found the same double-peak structure in 2017-08-16 and 2018-07-12 **with a simple contour analysis, but a more refined study showed only a single significant peak per night. Nevertheless, we did find a very strong variability of the signal from one transit to another, that confirms the results from the line profile tomography.**

To conclude, we used different methods (line profile tomography and `FeI` CCFs) to find independently a high variability of the atmospheric signal of KELT-20b during different transits. We also confirm the blueshift of the `FeI` signal and the reliability of the atmospheric RML method to estimate the atmospheric extension.

Acknowledgements. This work has made use of the VALD database, operated at Uppsala University, the Institute of Astronomy RAS in Moscow, and the University of Vienna. MB acknowledges support from the UK Science and Technology Facilities Council (STFC) research grant ST/S000631/1. GSc acknowledges the funding support from Italian Space Agency (ASI) regulated by "Accordo ASI-INAF n. 2013-016-R.0 del 9 luglio 2013 e integrazione del 9 luglio 2015".

References

Asplund, M., Grevesse, N., Sauval, A. J., & Scott, P. 2009, ARA&A, 47, 481
Bell, T. J. & Cowan, N. B. 2018, ApJ, 857, L20
Borsa, F., Allart, R., Casasayas-Barris, N., et al. 2020, arXiv e-prints, arXiv:2011.01245
Borsa, F., Rainer, M., Bonomo, A. S., et al. 2019, A&A, 631, A34
Bourrier, V., Ehrenreich, D., Lendl, M., et al. 2020, A&A, 635, A205
Brogi, M. & Line, M. R. 2019, AJ, 157, 114
Cabot, S. H. C., Madhusudhan, N., Welbanks, L., Piette, A., & Gandhi, S. 2020, MNRAS, 494, 363
Casasayas-Barris, N., Pallé, E., Yan, F., et al. 2018, A&A, 616, A151
Casasayas-Barris, N., Pallé, E., Yan, F., et al. 2019, A&A, 628, A9
Cegla, H. M., Lovis, C., Bourrier, V., et al. 2016, A&A, 588, A127
Claudi, R., Benatti, S., Carleo, I., et al. 2016, in Society of Photo-Optical Instrumentation Engineers (SPIE) Conference Series, Vol. 9908, Proc. SPIE, 99081A
Cosentino, R., Lovis, C., Pepe, F., et al. 2012, in Society of Photo-Optical Instrumentation Engineers (SPIE) Conference Series, Vol. 8446, Proc. SPIE, 84461V
Cosentino, R., Lovis, C., Pepe, F., et al. 2014, in Society of Photo-Optical Instrumentation Engineers (SPIE) Conference Series, Vol. 9147, Proc. SPIE, 91478C
Covino, E., Esposito, M., Barbieri, M., et al. 2013, A&A, 554, A28
Czesla, S., Schröter, S., Schneider, C. P., et al. 2019, PyA: Python astronomy-related packages
Deetjen, J. L. 2000, A&A, 360, 281
Delrez, L., Santerne, A., Almenara, J. M., et al. 2016, MNRAS, 458, 4025
Dimitriadis, G., Rojas-Bravo, C., Kilpatrick, C. D., et al. 2019, ApJ, 870, L14
Donati, J. F., Semel, M., Carter, B. D., Rees, D. E., & Collier Cameron, A. 1997, MNRAS, 291, 658
Dravins, D., Lindegren, L., & Torkelsson, U. 1990, A&A, 237, 137
Ehrenreich, D., Lovis, C., Allart, R., et al. 2020, Nature, 580, 597
Ehrenreich, D., Tinetti, G., Lecavelier Des Etangs, A., Vidal-Madjar, A., & Selsis, F. 2006, A&A, 448, 379
Ehrenreich, D., Vidal-Madjar, A., Widemann, T., et al. 2012, A&A, 537, L2
Fleig, J., Rauch, T., Werner, K., & Kruk, J. W. 2008, A&A, 492, 565
Foreman-Mackey, D., Hogg, D. W., Lang, D., & Goodman, J. 2013, PASP, 125, 306
Gray, D. F. 2008, The Observation and Analysis of Stellar Photospheres
Guilluy, G., Andretta, V., Borsa, F., et al. 2020, arXiv e-prints, arXiv:2005.05676
Heng, K. & Showman, A. P. 2015, Annual Review of Earth and Planetary Sciences, 43, 509
Hoeijmakers, H. J., Cabot, S. H. C., Zhao, L., et al. 2020, arXiv e-prints, arXiv:2004.08415
Hoeijmakers, H. J., Ehrenreich, D., Heng, K., et al. 2018, Nature, 560, 453
Hoeijmakers, H. J., Ehrenreich, D., Kitzmann, D., et al. 2019, A&A, 627, A165
Høg, E., Fabricius, C., Makarov, V. V., et al. 2000, A&A, 355, L27
Lothringer, J. D. & Barman, T. 2019, ApJ, 876, 69
Lund, M. B., Rodriguez, J. E., Zhou, G., et al. 2017, AJ, 154, 194
McLaughlin, D. B. 1924, ApJ, 60, 22
Nugroho, S. K., Gibson, N. P., de Mooij, E. J. W., et al. 2020, arXiv e-prints, arXiv:2003.04856
Ohta, Y., Taruya, A., & Suto, Y. 2005, ApJ, 622, 1118
Oliva, E., Origlia, L., Maiolino, R., et al. 2012, in Society of Photo-Optical Instrumentation Engineers (SPIE) Conference Series, Vol. 8446, Proc. SPIE, 84463T
Origlia, L., Oliva, E., Baffa, C., et al. 2014, in Society of Photo-Optical Instrumentation Engineers (SPIE) Conference Series, Vol. 9147, Proc. SPIE, 91471E
Parmentier, V., Line, M. R., Bean, J. L., et al. 2018, A&A, 617, A110
Pino, L., Désert, J.-M., Brogi, M., et al. 2020, ApJ, 894, L27
Pino, L., Ehrenreich, D., Wyttenbach, A., et al. 2018, A&A, 612, A53
Piskunov, N. E., Kupka, F., Ryabchikova, T. A., Weiss, W. W., & Jeffery, C. S. 1995, A&AS, 112, 525
Rainer, M., Poretti, E., Mistò, A., et al. 2016, AJ, 152, 207
Reiners, A. & Schmitt, J. H. M. M. 2002, A&A, 384, 155
Rossiter, R. A. 1924, ApJ, 60, 15
Ryabchikova, T., Piskunov, N., Kurucz, R. L., et al. 2015, Phys. Scr, 90, 054005
Sadeghi, M. & Behnia, F. 2018, arXiv e-prints, arXiv:1808.10489
Savitzky, A. & Golay, M. J. E. 1964, Analytical Chemistry, 36, 1627
Smith, M. A. & Gray, D. F. 1976, PASP, 88, 809
Stangret, M., Casasayas-Barris, N., Pallé, E., et al. 2020, arXiv e-prints, arXiv:2003.04650
Stock, J. W., Kitzmann, D., Patzer, A. B. C., & Sedlmayr, E. 2018, MNRAS, 479, 865
Talens, G. J. J., Justesen, A. B., Albrecht, S., et al. 2018, A&A, 612, A57
Van Rossum, G. & Drake Jr, F. L. 1995, Python tutorial (Centrum voor Wiskunde en Informatica Amsterdam, The Netherlands)

[1] INAF - Osservatorio Astrofisico di Arcetri, Largo Enrico Fermi 5, I-50125 Firenze, Italy
e-mail: `monica.rainer@inaf.it`
[2] INAF - Osservatorio Astronomico di Brera, Via E. Bianchi, 46, I-23807 Merate (LC), Italy
[3] Anton Pannekoek Institute for Astronomy, University of Amsterdam Science Park 904 1098 XH Amsterdam, The Netherlands
[4] Università degli Studi di Milano Bicocca, Piazza dell'Ateneo Nuovo, 1, I-20126 Milano, Italy
[5] Department of Physics, University of Warwick, Coventry CV4 7AL, UK
[6] INAF - Osservatorio Astrofisico di Torino, Via Osservatorio 20, I-10025 Pino Torinese (TO), Italy
[7] Centre for Exoplanets and Habitability, University of Warwick, Gibbet Hill Road, Coventry CV4 7AL, UK
[8] INAF - Osservatorio Astronomico di Roma, Via Frascati 33, I-00078 Monte Porzio Catone (Roma), Italy
[9] Astronomy Department and Van Vleck Observatory, Wesleyan University, Middletown, CT 06459, USA
[10] INAF - Osservatorio Astronomico di Padova, Vicolo dell'Osservatorio, 5, I-35122 Padova (PD), Italy
[11] INAF - Osservatorio Astrofisico di Catania, Via S.Sofia 78, I-95123 Catania, Italy
[12] INAF - Osservatorio Astronomico di Palermo, Piazza del Parlamento, 1, I-90134 Palermo, Italy
[13] Department of Physics, University of Rome "Tor Vergata", Via della Ricerca Scientifica 1, I-00133, Rome, Italy
[14] Max Planck Institute for Astronomy, Königstuhl 17, D-69117, Heidelberg, Germany
[15] Department of Astronomy, University of Geneva, Chemin des Maillettes 51, CH-1290 Versoix, Suisse
[16] INAF - Osservatorio Astronomico di Capodimonte, Salita Moiariello 16, I-80131 Napoli, Italy
[17] INAF - Fundación Galileo Galilei, Rambla José Ana Fernandez Pérez 7, 38712 Breña Baja (TF), Spain
[18] INAF - Osservatorio Astronomico di Cagliari, Via della Scienza 5, I-09047 Cuccuru Angius, Selargius (CA), Italy
[19] INAF - Osservatorio Astronomico di Trieste, Via Giambattista Tiepolo, 11, I-34131 Trieste, Italy
[20] Aix-Marseille Université, CNRS, CNES, LAM, Marseille, France
[21] Dipartimento di Fisica e Astronomia Galileo Galilei – Università di Padova, Vicolo dell'Osservatorio 2, I-35122, Padova, Italy

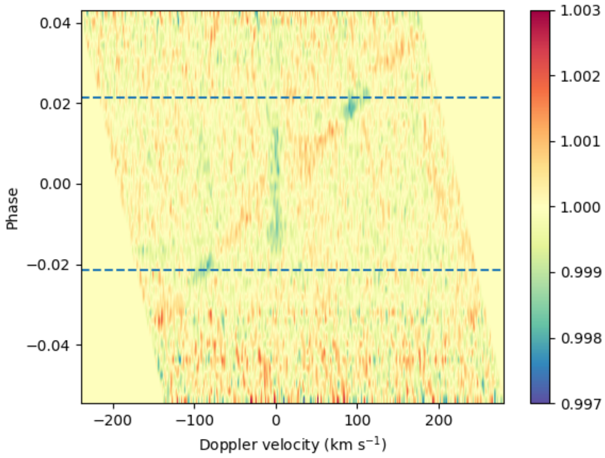

Fig. A.1. Line profile residuals after the Doppler shadow removals, and after being shifted in the planet reference frame. The atmospheric trace is clearly visible and centered around 0 km s^{-1}. There is still a visible Doppler shadow residual.

Appendix A: Atmospheric trace analysis on dataset B

In order to ensure that the removal of the Doppler shadow did not unduly affect the study of the atmospheric trace, we performed the removal with two methods, which generated two datasets. While the results from dataset A are shown in the paper, we show here the same analysis performed on dataset B.

The line profile residuals after the Doppler shadow's removal are shifted in the planetary reference frame and shown in Fig. A.1). It is clearly evident that the Doppler shadow's removal was less efficient in this case than in dataset A (see Fig. 7), as evidenced by the large residuals left in the tomography.

We smoothed each in transit residuals by applying a 3^{rd} degree Savitzky-Golay filter with a 15 pixels window. We then fitted the atmospheric signal using MCMC with a correlated noise model (see Fig. A.2).

The resulting RVs, FWHMs and depths are shown in Fig. A.3. As for dataset A, we found a blueshift during egress, while the FWHM is more stable (aside from the same outlier found in dataset A) and the depth shows a symmetric increase and subsequent decrease during transit.

We studied the overall variations during transit by averaging all residuals in the first and second half of the transit (phases [-0.02:0.0] and [0.0:0.02]), see Fig. A.4. We found a decrease of the overall FWHM, while RVs and depth are more stable. We performed the same study also on each individual night (see Fig. A.5). As for the results of dataset A, we found a small blueshift on 2018-07-12, and redshifts on 2019-08-26, and 2019-09-02, while the RVs is comparable within 1-σ on 2017-08-16, and 2018-07-19. The depth is stable during the transits, aside from 2019-08-26, where the signal became more shallow from the first to the second part of the transit. The FWHM decreases during the transit in four nights out of five, with the sole exception of 2018-07-12, where it shows the opposite behaviour.

The results are qualitatively identical to those obtained with dataset A, showing that the choice of the Doppler shadow removal method does not influence our work.

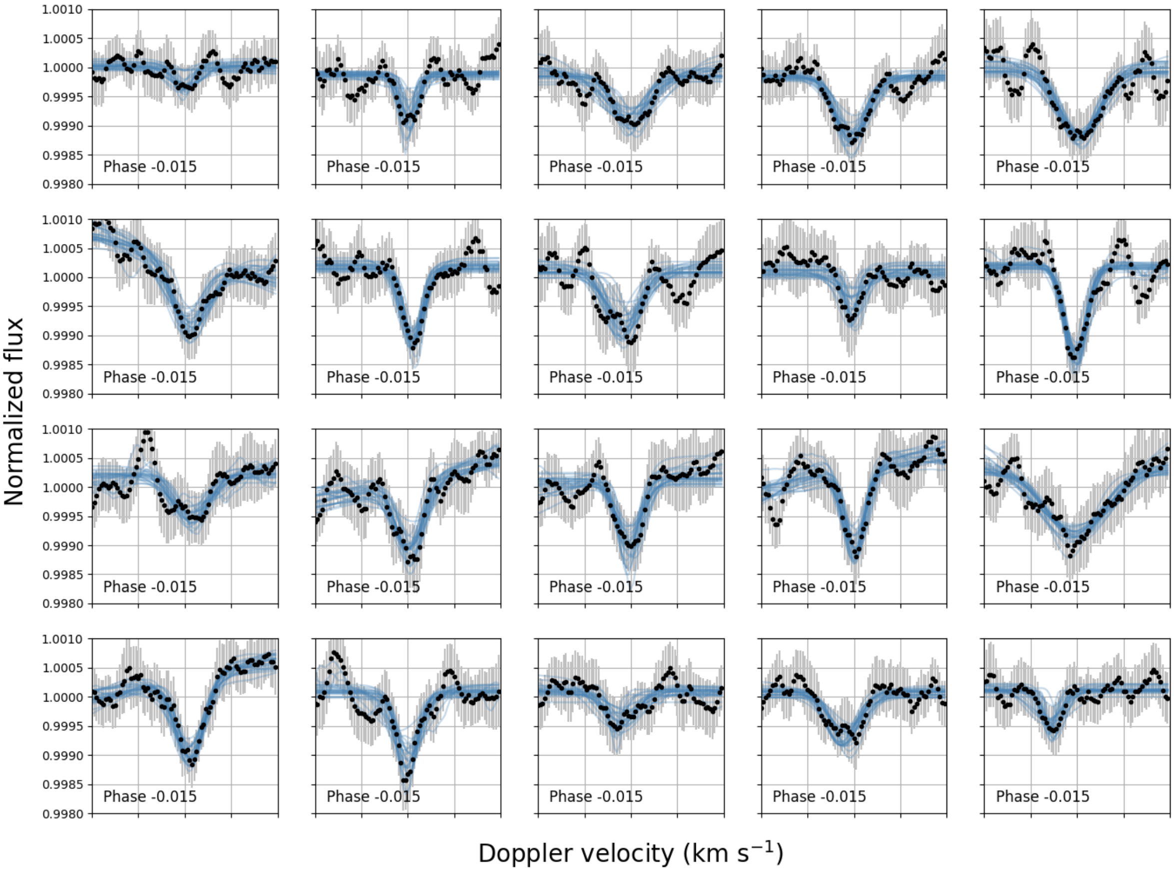

Fig. A.2. Atmospheric signal and relative MCMC posteriors. All the graphics have the same abscissa (RVs from -40 to 40 km s^{-1}) and ordinate (normalized flux from 0.998 to 1.001) to better follow the evolution of the signal. The graphics go from phase -0.019 (upper left panel) to phase 0.019 (lower right panel) with a 0.002 phase step.

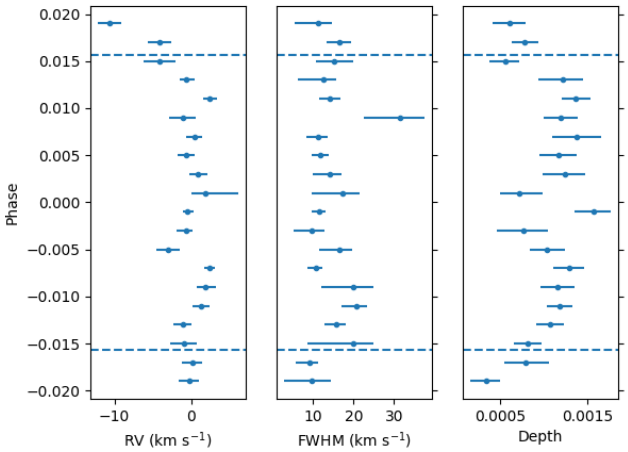

Fig. A.3. RVs, FWHM and depth of the atmospheric signal during transit. All the data are comprised between t_0 (start of ingress) and t_2 (end of egress), while the dashed lines indicate t_2 (end of ingress) and t_3 (start of egress)

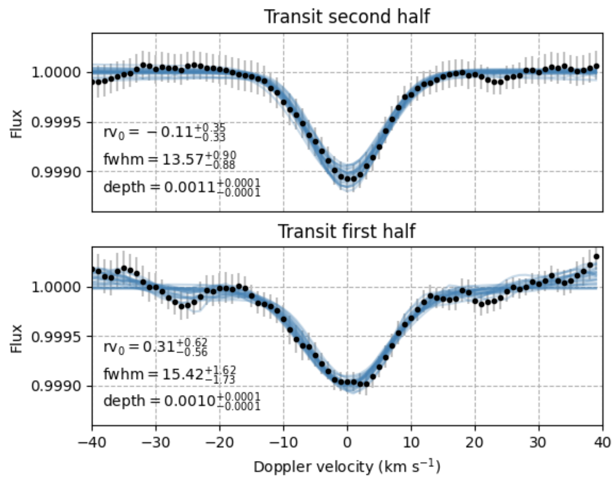

Fig. A.4. Averaged atmospheric signal in the first (phase [-0.02:0.0]) and second part (phase [0.0:0.02]) of the transit **with relative fit.**

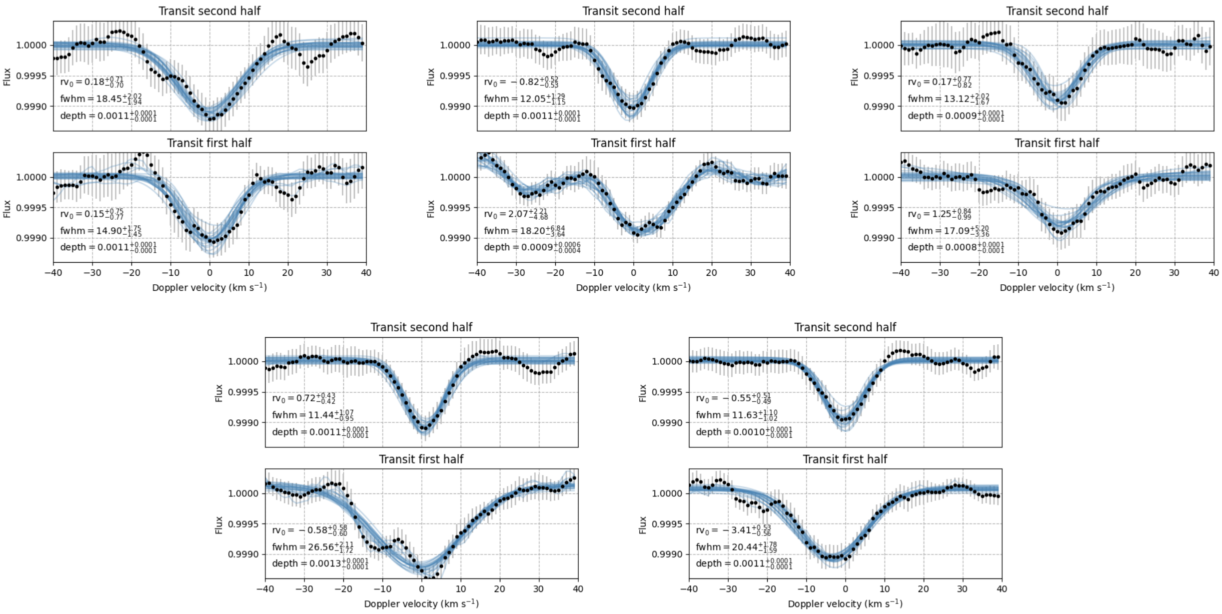

Fig. A.5. Averaged atmospheric signal in the first (phase [-0.02:0.0]) and second part (phase [0.0:0.02]) of each transit. From top left to bottom right, the graphics show the results for the nights 2017-08-16, 2018-07-12, 2018-07-19, 2019-08-26, and 2019-09-02.